

# Microscopic and Electronic Structure of Semimetallic Sb and Semiconducting AlSb Fabricated by Nanoscale Electrodeposition: An in Situ Scanning Probe Investigation

O. Mann, C. L. Aravinda, and W. Freyland\*

*Institute of Physical Chemistry, Karlsruhe University, Kaiserstrasse 12, 76128 Karlsruhe, Germany*

*Received: July 12, 2006; In Final Form: August 25, 2006*

The nanoscale electrocrystallization of pure Sb and the compound semiconductor AlSb on Au(111) has been studied by in situ scanning probe techniques (STM and STS) employing an ionic liquid electrolyte,  $\{\text{AlCl}_3\text{--}[\text{C}_4\text{mim}]^+\text{Cl}^-\}$  (1:1) containing  $\text{SbCl}_3$ . The characteristic changes of the electronic structures with varying potentials have been probed for the first time by normalized differential conductance spectra,  $(dI/dU)/(I/U)$ . In the underpotential deposition range of Sb the formation of two layers is observed. For the first monolayer a  $(\sqrt{3} \times \sqrt{3})R30^\circ$  structure is determined from atomically resolved STM images. During the deposition and dissolution of the Sb monolayers characteristic wormlike or spinodal structures appear indicating surface alloying of antimony with the gold substrate. Under overpotential conditions two different Sb structures have been observed. If the deposition potential is continuously stepped to  $-0.1$  V, Sb nanostripes form. On the other hand, randomly dispersed small clusters occur if the potential is jumped from  $0.0$  to  $-0.3$  V vs Al/Al(III). Both modifications exhibit typical semimetallic behavior as shown by the STS spectra. At  $-1.1$  V the cyclic voltammogram shows a clear reduction wave that is assigned to AlSb compound formation. Deposits in this potential range are characterized by a homogeneous distribution of clusters with diameters of  $\sim 20$  nm. Conductance spectra of these clusters exhibit the main features of the electronic structure of the bulk semiconductor AlSb, with a band gap of  $2.0 \pm 0.2$  eV. Electrodeposition experiments on both sides of the compound deposition potential show a strong doping effect that is manifest in the corresponding conductance spectra.

## Introduction

In recent years metal and semiconductor nanostructures have attracted considerable interest in science and technology. On the fundamental side this is motivated by the specific size-dependent thermodynamic, mechanical, and electronic properties of materials on the nanometer scale. On the other hand, they are basic for the construction of functional units in nanotechnology. The majority of functional nanostructures are fabricated by molecular beam epitaxy and similar vacuum deposition techniques, but also electrochemical scanning probe methods such as in situ scanning tunneling microscopy have been applied, see, e.g., refs 1–6. The latter were first developed for applications with aqueous electrolytes.<sup>4–6</sup> Extension of this technique of nanoscale electrodeposition with ionic liquid electrolytes has the advantage that they possess large electrochemical windows and thus a larger range of materials such as transition metals or compound semiconductors are accessible. Examples where this has been demonstrated recently are Ti nanowires or nanowire grids<sup>7</sup> on HOPG and quite recently AlSb clusters on Au(111).<sup>8</sup>

The electrochemical fabrication of compound semiconductors is still a challenging topic. Within the family of III–V compound semiconductors, the binary semiconductor AlSb shows promise as a highly efficient solar cell material.<sup>9</sup> However, its semiconducting properties are not well exploited for device applications owing to difficulties in fabricating the high-melting compound ( $T_m = 1058$  °C) by conventional techniques.<sup>9</sup> Its band structure, calculated by the LCAO method

in the local density approximation,<sup>10</sup> exhibits a direct gap of 2.5 eV and an indirect gap of 1.2 eV, the corresponding experimental values being 2.4 and 1.8 eV, respectively.<sup>11</sup> According to band structure calculations the density of states are rather symmetrical with reference to the Fermi level. This is confirmed by measurements of the conduction and valence band states of comparable III–V semiconductors employing tunneling spectroscopy.<sup>12</sup>

In a previous short communication we reported the first results of the nanoscale electrocrystallization of the binary semiconductor AlSb from an ionic liquid.<sup>8</sup> In this contribution we present a more detailed investigation of the electrochemical phase formation of this compound in the ionic liquid  $\{\text{AlCl}_3\text{--}[\text{C}_4\text{mim}]^+\text{Cl}^-\}$  (1:1) containing  $\text{SbCl}_3$  by in situ STM measurements. Furthermore, we have studied the doping of AlSb by excess Al and Sb varying the deposition potential on both sides of the compound semiconductor deposition potential. In addition, we have probed the structural changes of pure Sb deposition in the under- and overpotential range. Emphasis is given in the following to in situ tunneling spectroscopy (STS) measurements which enable a first insight into the changes of the electronic structure with varying deposition potential.

## Experimental Section

The electrochemical and in situ STM investigations were performed with an ionic liquid electrolyte. 1-Butyl-3-methylimidazolium chloride ( $[\text{C}_4\text{mim}]^+\text{Cl}^-$ ) was prepared from 1-chlorobutane and 1-methylimidazole (both from Merck) and purified by recrystallization from acetonitrile. Anhydrous  $\text{AlCl}_3$  (Fluka, >99%) was sublimated three times and stored under

\* Address correspondence to this author. Fax: ++49 721 608 6662. E-mail: werner.freyland@chemie.uni-karlsruhe.de.

vacuum prior to use. Under inert atmosphere (argon with  $\text{O}_2$  and  $\text{H}_2\text{O}$  concentration  $<1$  ppm),  $\text{AlCl}_3$  and  $[\text{C}_4\text{mim}]^+\text{Cl}^-$  crystals were mixed in an equal molar ratio yielding a colorless liquid (or slightly yellowish depending on the purity of the products). A viscous  $\text{SbCl}_3$ - $[\text{C}_4\text{mim}]^+\text{Cl}^-$  melt was obtained by mixing  $\text{SbCl}_3$  (Alfa,  $>99.99\%$ ) with  $[\text{C}_4\text{mim}]^+\text{Cl}^-$  in a 45:55 molar ratio. The effective  $\text{Sb(III)}$  concentration was prepared by adding the appropriate amount of  $\text{SbCl}_3$ - $[\text{C}_4\text{mim}]^+\text{Cl}^-$  to the  $\text{AlCl}_3$ - $[\text{C}_4\text{mim}]^+\text{Cl}^-$  (1:1) melt and then stirring for 24 h. A 200–300 nm Au(111) film evaporated on borosilicate glass covered by chromium (12 mm  $\times$  12 mm, Berliner Glas KG, Germany) was used as the working electrode. Prior to use, the substrate was annealed in a hydrogen flame for 3 min and then slowly cooled under a nitrogen stream (Griesheim, 5 N).

Electrochemical measurements were performed in a traditional three-electrode cell with Al wires used as reference and counter electrodes. In this article all potentials were measured versus the quasireference electrode Al/Al(III). Cyclic voltammograms (CVs) were recorded with an AutoLab potentiostat (PGSTAT 30, Eco Chemie, The Netherlands).

In situ scanning tunneling microscopy (STM) measurements were carried out in both constant current and height modes, using a Molecular Imaging (MI) controller. For the STM experiments, tunneling tips were freshly prepared from tungsten and Pt–Ir wires, followed by an electrochemical etching process in 2 mol·L<sup>-1</sup> NaOH aqueous solution and in 3.5 mol·L<sup>-1</sup> NaCN, respectively. Coating of the tips via electrophoresis with an epoxide electropaint (BASF ZQ 84-3225 0201, Germany) was performed to minimize the faradaic current. Because of the hygroscopic nature of the ionic liquid used, all the STM experiments were performed with a home-built microscope inside a vacuum tight stainless steel vessel filled with argon. The whole setup was installed on a vibration damping table and left for thermal stabilization prior to each experiment. For more details concerning assembly of the microscope and measurements under argon atmosphere, cf. ref 13.

Special care was taken to record tunneling spectra at different sites of the STM images and for clusters of different size. For this aim the  $I$ – $U$  curves were taken in the current imaging tunneling spectroscopy (CITS) mode<sup>14</sup> and were averaged over 5–10 measurements under constant conditions. From the differential  $I$ – $U$  curves the normalized differential conductance spectra  $(dI/dU)/(I/U)$  have been determined following the evaluation method described by Feenstra.<sup>12</sup>

## Results and Discussion

**Cyclic Voltammetry.** An overview of the redox processes occurring during antimony and the respective alloy electrodeposition from an  $\{\text{AlCl}_3$ - $[\text{C}_4\text{mim}]^+\text{Cl}^-\}$  (1:1) ionic liquid containing 2 mM  $\text{SbCl}_3$  at a Au(111) electrode obtained by cyclic voltammetry investigation is presented in Figure 1. All potentials are given with respect to an Al/Al(III) quasireference electrode. The reduction peak C1 at 0.55 V and its corresponding anodic peak A1 are well separated from the following processes. The amplitude of the peak changes roughly with the square root of the scan rate (see inset) and together with its slope indicates a reversible two-electron process of  $\text{Sb(V)}$  to  $\text{Sb(III)}$ .<sup>15</sup> The reduction peak C2 at 0.05 V we explain by the UPD process of Sb, which is confirmed by the STM results presented below. An interesting feature is observed for the corresponding anodic peak A2. Two different oxidation processes can be involved in this peak. The first one we attribute to the dissolution of the UPD of Sb and the second may be due to the oxidation of the acidic form of  $\text{Sb(III)}$  ( $\text{SbCl}_2^+$ ). Indeed, a small excess of  $\text{AlCl}_3$

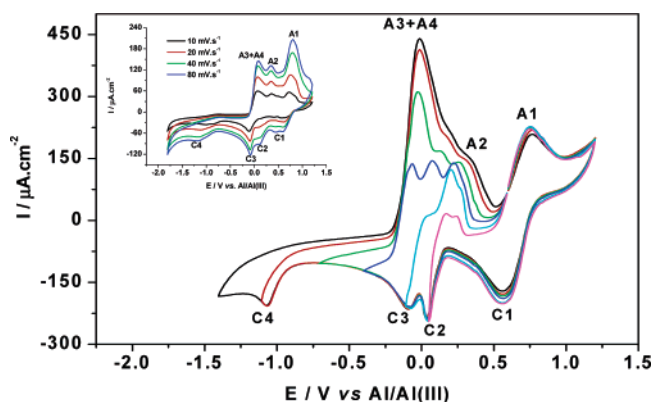


**Figure 1.** Cyclic voltammograms of 2 mM  $\text{SbCl}_3$ - $[\text{C}_4\text{mim}]^+\text{Cl}^-$  in a molar ratio of 45:55 in  $\text{AlCl}_3$ - $[\text{C}_4\text{mim}]^+\text{Cl}^-$  (1:1) on Au(111) at a scan rate of 100 mV s<sup>-1</sup> recorded at different reversal cathodic potential. The inset shows the cyclic voltammogram recorded in a melt containing 1 mM  $\text{Sb(III)}$  at different sweep rates of 10, 20, 40, and 80 mV s<sup>-1</sup> at room temperature.

added in a solution of  $\text{SbCl}_3$  in a neutral melt forms  $\text{SbCl}_2^+$  cations which can be reduced to  $\text{Sb}$ .<sup>16</sup> Thus, the peak C2 possibly involves two processes corresponding to the UPD and the deposition of the acidic form of  $\text{Sb}$ .<sup>8</sup> By reducing the potential to  $-0.10$  V (peak C3) the overpotential deposition of Sb is reached.<sup>17</sup> The corresponding dissolution peak A3 is observed at  $0.10$  V and it tends to increase and merge with the anodic peak A4 depending on the reversal deposition potential. At potentials negative of that of peak C3, Al and Sb co-deposition has to be considered, which finally leads to a clear peak C4 at  $-1.1$  V. This marks the formation of the stoichiometric  $\text{AlSb}$  semiconducting compound, which is evidenced by the STM and, in particular, the STS results. The corresponding anodic peak A4 increases continuously with decreasing potential and is attributed to the dissolution of co-deposited aluminum and  $\text{AlSb}$ .

Another interesting feature observed in the CVs is a little shift of approximately  $0.15$  V recorded for each experiment in comparison with previous studies.<sup>17</sup> The slight acidic characteristic of the melt can explain this observation. Indeed, a slight change of the ionic liquid acidity changes drastically the reduction potential so that  $\text{Sb(III)}$  reduction in acidic melts occurs at up to  $1$  V more positive potentials than in basic melts.<sup>15</sup>

**Underpotential Deposition of Sb.** STM results of the initial nucleation and growth process of the underpotential deposition of antimony from  $\{\text{AlCl}_3$ - $[\text{C}_4\text{mim}]^+\text{Cl}^-\}$  (1:1) ionic liquid containing 2 mM  $\text{SbCl}_3$  on Au(111) are shown in Figure 2. In the range of the open circuit potential ( $0.55$  V), bare gold terraces were imaged with atomic resolution (see Figure 2a). In the first minute after stepping the potential to  $0.2$  V, the Au(111) surface starts to be covered with small islands which correspond to the beginning of the Sb UPD whereby the islands are monatomically high and grow two-dimensionally. A layer of Sb starts to grow from the monatomic step edges as well as on the terraces of Au(111). By switching the potential toward  $0.15$  V (Figure 2b), the islands grow faster with a constant monatomic height and also start to merge with each other. The region marked by the dashed lines in the high-resolution image of the first layer of Sb acquired at  $0.15$  V (Figure 2c) shows a typical hexagonal structure that is confirmed by the 2D Fast Fourier Transformation (2D-FFT) shown in the inset of Figure 2c. The inverse 2D FFT of the high-resolution picture of the first Sb monolayer is presented in Figure 2d, which allows evaluating the lattice parameter more precisely. The unit cell parameters,  $a$  and  $b$ , are found to be equal to  $5.1 \pm 0.4$  Å ( $\sqrt{3}$



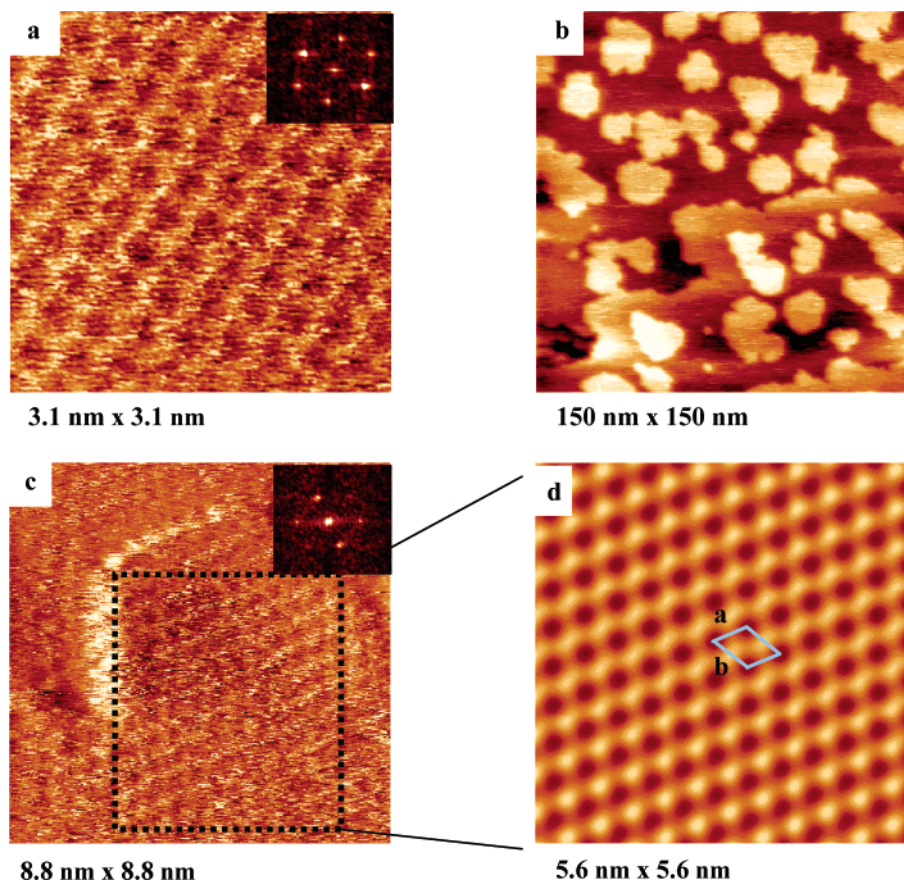


**Figure 2.** (a) Atomically resolved STM image of gold at 0.6 V,  $E_{\text{tip}} = 0.65$  V,  $I_t = 25$  nA. The inset shows the structure of Au(111) derived from the 2D FFT. (b) Large-scale STM image showing the formation of the first layer of antimony at 0.15 V,  $E_{\text{tip}} = 0.35$  V,  $I_t = 1$  nA. (c) High-resolution STM image of an antimony island at 0.15 V,  $E_{\text{tip}} = 0.3$  V,  $I_t = 25$  nA. The inset shows the 2D FFT region delimited by dotted lines in the STM image corresponding to lattice parameters of  $a = 5.1 \pm 0.4$  Å and  $b = 5.3 \pm 0.4$  Å. (d) Inverse 2D FFT of the high-resolution Sb monolayer picture showing a structure of  $(\sqrt{3} \times \sqrt{3})R30^\circ$ .

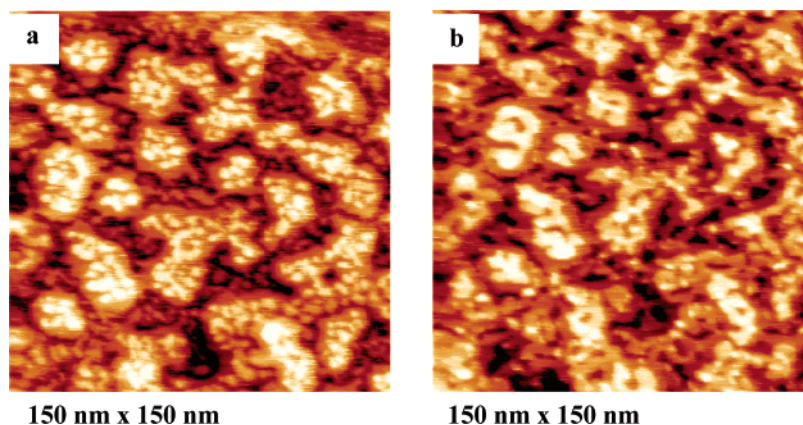


**Figure 3.** (a) Large-scale STM image showing the formation of the second Sb monolayer during the UPD process at 0.05 V,  $E_{\text{tip}} = 0.20$  V,  $I_t = 1$  nA and (b) after 15 min deposition at 0.0 V,  $E_{\text{tip}} = 0.2$  V,  $I_t = 1$  nA.

times the Au–Au interatomic distance) and  $5.3 \pm 0.4$  Å, respectively. According to the analysis of antimony and gold atomic resolution pictures, the Sb monolayer is rotated by  $30^\circ$  with respect to the bare gold surface, which is in good agreement with the  $(\sqrt{3} \times \sqrt{3})R30^\circ$  structure described in the literature for the adsorption of Sb on Cu(111)<sup>18</sup> and Au(111).<sup>19</sup> It is interesting to note that formation of 2D Sb-nanostripes with a  $(\sqrt{7} \times \sqrt{7})$  structure reported previously<sup>8</sup> could not be observed in the UPD region in this study. Since the ionic melts in the separate experiments were not identical, but differed in composition and acidity, this can have a strong impact on the reduction potentials and on anion adsorption and thus on the

UPD process. As a matter of fact, the CVs of both experiments exhibit a clear distinction in the UPD region.

Before the first Sb monolayer was completed, the potential was reduced toward more negative potentials leading to the formation of a second antimony layer (Figure 3). Indeed, after stepping the potential down to 50 mV, Sb continues to be deposited onto Au(111) to complete the first layer but now also grows on the top of large Sb islands starting the second monolayer. It is interesting to note that with increasing coverage of the first and second monolayer wormlike structures appear.

Figure 3a clearly shows small bright patches all over the surface either on the top of the Sb islands corresponding to the

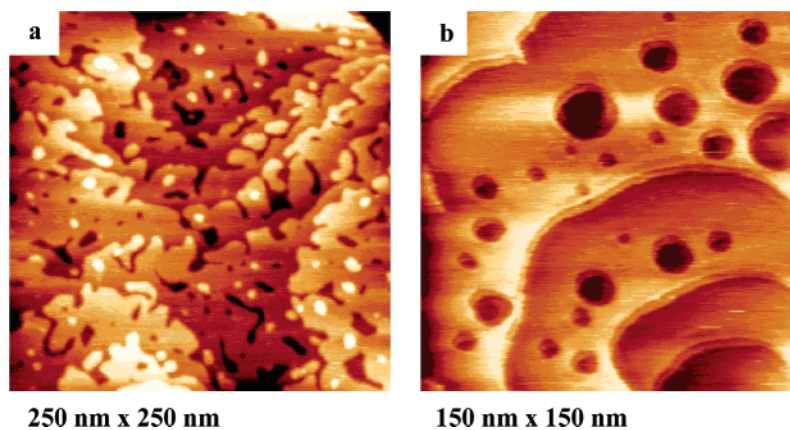


**Figure 4.** (a) Large-scale STM image showing an almost complete Sb monolayer formed from 2 mM  $\text{SbCl}_3\text{-}[\text{C}_4\text{mim}]^+\text{Cl}^-$  in a molar ratio of 45:55 in  $\text{AlCl}_3\text{-}[\text{C}_4\text{mim}]^+\text{Cl}^-$  solution at 0.12 V,  $E_{\text{tip}} = 0.37$  V,  $I_t = 1$  nA. (b) Morphology of the surface after 5 min of dissolution at 0.50 V,  $E_{\text{tip}} = 0.65$  V,  $I_t = 1$  nA; the corresponding STM image is obviously affected by the double-tip effect but nevertheless shows the evolution of large holes on dissolution.

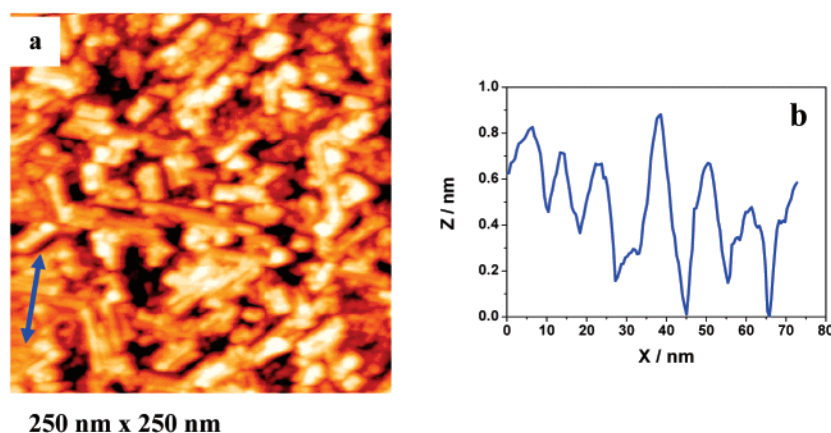


**Figure 5.** (a) Large-scale STM image showing a particular structure of 3D Sb growth at  $-0.1$  V,  $E_{\text{tip}} = 0.15$  V,  $I_t = 1$  nA. (b) Height profile of the associated area marked with an arrow on the STM image.

second layer or between them completing the first layer. In this early stage of the second layer formation small clusters seem to be deposited randomly on the surface yielding a disordered but again wormlike Sb deposit. Stepping the potential down to 0 V accelerates the growth of the existing islands and facilitates further nucleation of new islands as shown in Figure 3b. The first layer appears to be almost complete but wormlike structure pits (black spots) still remain. Bright spots observed on top of the second layer indicate the beginning of OPD.

**Surface Alloying.** Investigating the structure of the Sb monolayer during the dissolution process, the STM images exhibit a behavior that indicates a prior surface alloying in the Sb UPD range. Figure 4 illustrates the structure of the surface before and after applying an anodic potential. Switching the potential toward 0.12 V and keeping it constant for about 30 min yields an almost complete layer of Sb on the gold surface as presented in Figure 4a. This long polarization time is typical of the slow surface alloying kinetics.<sup>20</sup> By analyzing the results of this polarization in detail it clearly appears that the layer is not homogeneous, but contains characteristic wormlike defects typical of the spinodal decomposition structures of surface alloying.<sup>20</sup> Stepping the potential directly back to 0.5 V yields the gold surface features shown in Figure 4b. But now several monatomically deep holes of different size are observed all over the gold surface. Their evolution in time follows the classical Ostwald ripening law. Keeping the potential constant at 0.5 V for a long time ( $>45$  min) the gold surface heals until the holes completely disappear. This reflects the relatively high surface

diffusion of the Au adatoms which are expelled from the surface alloy during its dissolution. All these features lead to the conclusion that an Sb–Au surface alloy forms in the UPD region. This is consistent with previous studies on electrodeposition of Sb on Au(111).<sup>19</sup>

**Overpotential Deposition of Sb.** Switching the potential negative of 0 V, the OPD of Sb begins on top of the 2D adlayers. Depending on the Sb bulk deposition procedure, two different morphologies are observed. The first interesting topography is shown in Figure 5. If the potential is kept at a positive value around 0.12 V until a complete monolayer of Sb has formed (cf. Figure 4a) and then is continuously decreased below  $-0.1$  V, the 3D deposition process starts. The resulting STM picture is shown in Figure 5a. Two morphologies can be distinguished: a well-organized pattern of large elongated nanostripes and a more random distribution of elongated clusters on the remaining surface. The nanostripes are confined to a maximum height of  $1 \pm 0.2$  nm, a length of 30–35 nm, and a typical width of  $10 \pm 1$  nm, as shown in the profile in Figure 5b. This growth characteristic was still observed during the thickening of the deposit when the potential was stepped to more negative values. Similar features together with an invariance of the size of the Sb deposit has also been observed in the study of Sb deposition on Cu(100) from aqueous solution.<sup>19</sup>

The second interesting structure, shown in Figure 6, has been obtained with the following electrodeposition procedure. Instead of keeping the potential constant until a complete monolayer is formed, the potential has been continuously decreased with a



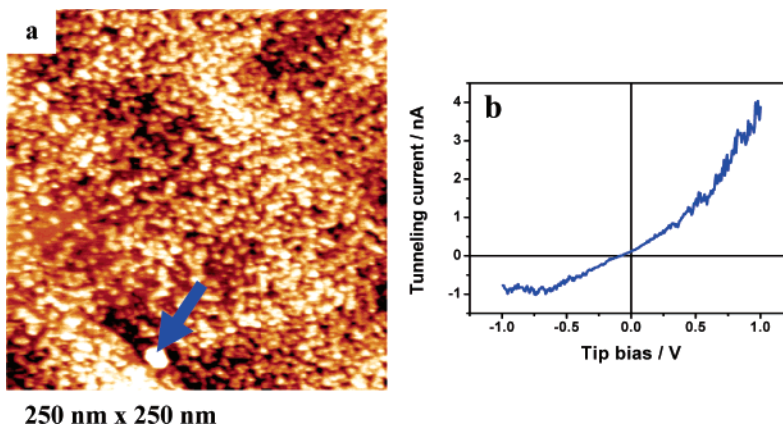


**Figure 6.** (a) Sb OPD process at  $-0.30$  V,  $E_{\text{tip}} = -0.15$  V,  $I_t = 1$  nA. (b) Typical  $I-U$  tunneling spectra for pure Sb in the OPD range (the arrow indicates the tip position during the spectra acquisition).

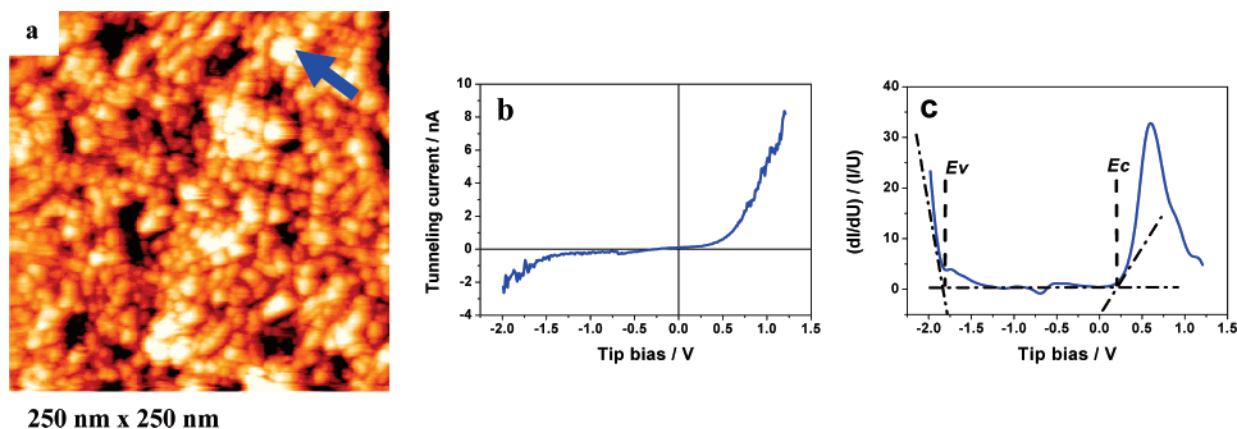


**Figure 7.** (a) Large-scale STM image after switching the potential to  $-1.2$  V,  $E_{\text{tip}} = -0.75$  V,  $I_t = 1$  nA showing the growth of the  $\text{Al}_x\text{Sb}_{1-x}$  alloy. (b) STS spectrum recorded for the cluster indicated with an arrow on the STM image. (c) Normalized differential conductivity spectrum of the cluster marked with an arrow on the STM image.

rate of  $0.20$  V per scan from the UPD region to zero potential and then has been directly jumped to  $-0.30$  V. Under this condition, smaller clusters are produced randomly distributed all over the surface as presented in Figure 6a. In this case, antimony grows three-dimensionally by the Stransky–Krastanov mode whereby slightly elongated clusters deposit all over the surface. The associated STS spectrum given in Figure 6b shows the electronic structure of the cluster marked with an arrow on the STM image. The shape of the  $I-U$  curve clearly shows semimetallic behavior. In the positive tip bias direction the tunneling current raises continuously whereas in the negative direction the tunneling current seems to reach a minimum, which indicates the asymmetrical behavior of the  $I-U$  curve. These observations confirm the presence of a semimetallic deposit as expected in the case of pure Sb.

**Electrocrystallization of the Stoichiometric Compound Semiconductor AlSb.** The cyclic voltammogram in Figure 1 exhibits a pronounced reduction peak at  $-1.1$  V that we provisionally assigned to the formation of the AlSb compound. Thermodynamically this is a very stable compound with a high melting point of  $1058$  °C.<sup>9</sup> Results of STM and STS measurements in this potential range are shown in Figure 7. The STM image shows a nearly random distribution of clusters with a size ranging from  $\sim 10$  to  $25$  nm. In addition, several elongated clusters with a length up to  $\sim 30$  nm are visible. With this size of clusters it is reasonable to assume that they represent already the bulk electronic properties. This, indeed, is seen in the STS spectrum. An example of an  $I-U$  curve recorded at the spherical cluster of  $\sim 25$  nm diameter marked in Figure 7a is given in

Figure 7b. This experimental data set indicates a voltage gap of  $\sim 1.8$  V. Further analysis of the  $I-U$  curves by the method of Feenstra<sup>22</sup> to obtain the normalized differential conductance spectra,  $(dI/dU)/(I/U)$ , is shown in Figure 7c. Determining the band onset positions as indicated by the extrapolations in Figure 7c, one obtains for the separation of the valence band edge,  $E_v$ , and conduction band edge,  $E_c$ , a value of  $2.0 \pm 0.2$  eV, which within experimental errors is in agreement with the experimental indirect gap energy of bulk AlSb, which ranges from  $1.7$  eV<sup>23</sup> to  $1.87$  eV.<sup>11</sup> The energy dependence of the density of states above  $E_c$  and below  $E_v$  is nearly symmetrical in accordance with band structure calculations.<sup>10</sup> Above  $E_v$  a relatively high density of dopant induced states is visible possibly due to deviations from the stoichiometric compound AlSb. According to the cyclic voltammogram the latter is expected at a deposition potential of  $-1.1$  V, whereas the data in Figure 7 correspond to a sample that has been deposited at  $-1.2$  V. Striking is the position of the Fermi-level  $E_F$ , which corresponds to the zero of bias voltage. It is shifted toward the conduction band edge. A similar trend is observed in III–V semiconductors with n-doping.<sup>12</sup>

**Electrodeposition off of Stoichiometric AlSb.** To study the effect of doping on the homogeneity of the deposits and their electronic structure we performed electrodeposition experiments on both sides of the compound deposition potential of  $-1.1$  V. In Figure 8a,b we compare the STM images on a large scale of two deposits recorded at deposition potentials of  $-0.9$  and  $-1.5$  V, respectively. In the first case, which represents deposition

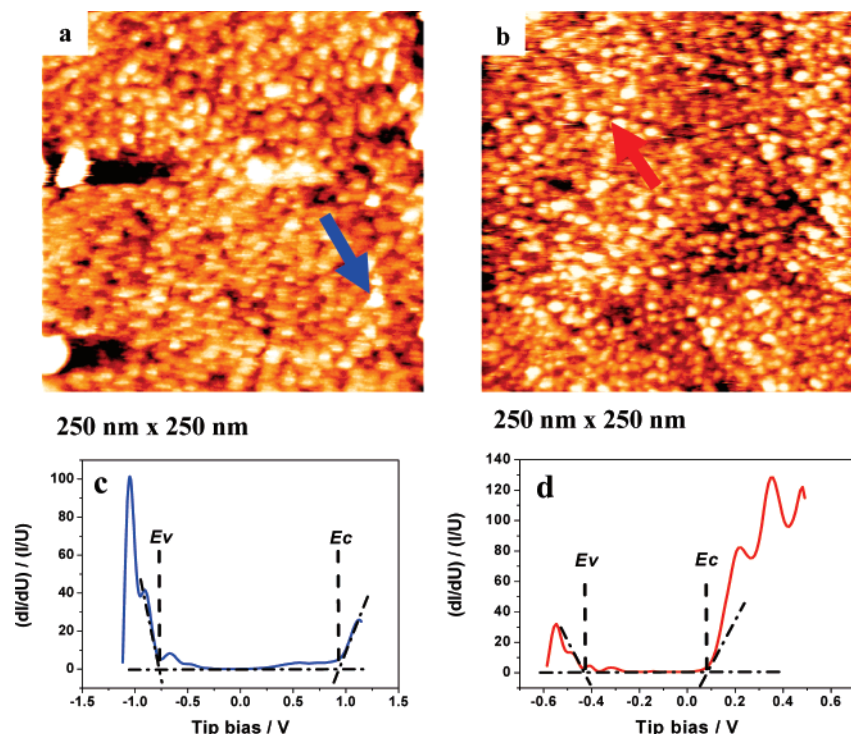


**Figure 8.** (a) Large-scale STM image showing the beginning of the  $\text{Al}_x\text{Sb}_{1-x}$  alloy formation at  $-0.9$  V,  $E_{\text{tip}} = -0.55$  V,  $I_t = 1$  nA. (b) Large-scale STM image after switching the potential toward  $-1.5$  V,  $E_{\text{tip}} = -0.85$  V,  $I_t = 1$  nA showing the beginning of Al bulk deposition on  $\text{Al}_x\text{Sb}_{1-x}$ . (c and d) The respective normalized differential conductivity spectra of the clusters marked by arrows in the STM images where  $I/V$  has been broadened with a one-pole Fourier low-pass filter.

conditions on the antimony-rich side, a homogeneous coverage of the surface by clusters of comparable size is evident. The two exceptionally big clusters are discussed separately below. In contrast to this, the cluster size distribution clearly changes for the deposit at  $-1.5$  V where a large fraction of small clusters appears. This behavior is typical of aluminum alloy deposition like  $\text{Al-Ni}$ <sup>24</sup> or  $\text{Al-Co}$ .<sup>25</sup> This difference in the topography of deposition at Al-rich and Sb-rich conditions is strongly reflected in the corresponding conductance spectra, Figure 8c,d. In the Sb-rich case, a strong enhancement of valence band states is observed, whereas on the Al-rich side the conduction band states are increased by roughly a factor of 5 with respect to the pure  $\text{AlSb}$  compound. In the latter case, also, the size of the band gap seems to be strongly reduced. Not knowing the role of surface states it is difficult to discuss the structures indicated in the respective conduction and valence bands.

The spectra given in Figure 8c,d have been recorded for different clusters of comparable size as seen in the corresponding STM images in Figure 8a,b. In one example we have studied the effect of cluster size on the conductance spectra. For this aim we selected the two big clusters located at the left part of Figure 8a. For these big clusters we find a spectrum that resembles that in Figure 8d, i.e., representing Al-rich deposition conditions. This example indicates that during electrodeposition inhomogeneities may occur presumably due to differences in the nucleation and growth process at specific sites.

## Summary and Conclusions

The electrocrystallization of pure Sb and the compound semiconductor  $\text{AlSb}$  have been investigated by in situ STM and STS measurements in a wide range of deposition potentials from  $-1.5$  to  $+1.2$  V. This was made possible by employing an ionic liquid, the  $\{\text{AlCl}_3\text{-}[\text{C}_4\text{mim}]^+\text{Cl}^-\}$  (1:1) melt containing  $\text{SbCl}_3$ , and thus taking advantage of the large electrochemical window of this melt.

In the underpotential deposition range 2D electrocrystallization of pure Sb is characterized by a layer-by-layer growth mechanism. The first monolayer of Sb on  $\text{Au}(111)$  has been imaged with atomic resolution yielding the typical  $(\sqrt{3} \times \sqrt{3})R30^\circ$  structure. During deposition and dissolution of the Sb monolayers characteristic wormlike or spinodal structures appear indicating surface alloying of antimony with the gold substrate. Depending on the deposition procedure two different Sb structures have been obtained at overpotential conditions. Stepping the deposition potential continuously toward  $-0.1$  V, Sb nanostripes can be formed. Jumping the potential from zero potential to  $-0.3$  V, randomly dispersed small clusters are observed. The STS spectra analysis of these clusters shows typical semimetallic behavior. Near the  $\text{AlSb}$  deposition potential of ca.  $-1.1$  V a homogeneous distribution of clusters with sizes up to 25 nm is found. Their electronic structure, analyzed by STS and the corresponding conductance spectra, is characterized by the main electronic features of the bulk compound semiconductor  $\text{AlSb}$ , e.g., a gap energy of  $\sim 2.0$  eV. Strong doping effects have been observed in the conductance spectra taken on deposits which have been fabricated at potentials off of the compound deposition potential. At  $-1.5$  V, where Al deposition dominates, the conduction band density of states is strongly enhanced. On the other hand, at  $-0.9$  V a pronounced increase of the valence band density of states relative to that of the stoichiometric  $\text{AlSb}$  compound is found. In summary, these investigations show for the first time that nanoscale fabrication of large-gap compound semiconductors including their doping is possible by electrochemical means with use of ionic liquid electrolytes.

**Acknowledgment.** The authors acknowledge financial support of this project by the DFG Center of Functional Nanostructures (CFN) at the University of Karlsruhe.

## References and Notes

- (1) Shchuki, V. A.; Lebentsov, N. N.; Bimberg, D. *Epitaxy of Nanostructures*; Springer: Berlin, 2004.
- (2) Teichert, C. *Phys. Rep.* **2002**, *365*, 335.
- (3) Ledentsov, N. N. Growth Processes and Surface Phase Equilibria in Molecular Beam Epitaxy. In *Springer Tracts in Modern Physics*; Springer: Berlin, Germany, 1999.
- (4) Magnussen, O. M.; Hotlos, J.; Nichols, R. J.; Kolb, D. M.; Behm, R. J. *Phys. Rev. Lett.* **1990**, *64*, 2929.
- (5) Manne, S.; Hansma, P. K.; Massie, J.; Elings, V. B.; Gewirth, A. A. *Science* **1991**, *251*, 183.
- (6) Hachiya, T.; Honbo, H.; Itaya, K. *J. Electroanal. Chem.* **1991**, *315*, 275.
- (7) Mukhopadhyay, I.; Freyland, W. *Langmuir* **2003**, *19*, 1951.
- (8) Aravinda, C. L.; Freyland, W. *Chem. Commun.* **2006**, *16*, 1703.
- (9) (a) Ang, C. Y.; Lacy, L. L. *Metall. Trans. A* **1979**, *10*, 519. (b) Pino, R.; Ko, Y.; Dutta P. S. *J. Cryst. Growth* **2006**, *290*, 29.
- (10) Huang, M. Z.; Ching, W. Y. *Phys. Rev. B* **1993**, *47*, 9449.
- (11) Barker, A. S. *Phys. Rev.* **1968**, *165*, 917.
- (12) Feenstra, R. M. *Phys. Rev. B* **1994**, *50*, 4561.
- (13) Shkurankov, A.; Endres, F.; Freyland, W. *Rev. Sci. Instrum.* **2002**, *73*, 102.
- (14) Weitering, H. H.; Carpinelli, J. M. *Surf. Sci.* **1997**, *384*, 240.
- (15) Yang, M.-H.; Sun, I.-W. *J. Appl. Electrochem.* **2003**, *33*, 1077.
- (16) Lipsztajn, M.; Osteryoung, R. A. *Inorg. Chem.* **1985**, *24*, 3492.
- (17) Habboush, D. A.; Osteryoung, R. A. *Inorg. Chem.* **1984**, *23*, 1726.
- (18) Ward, L. C.; Stickney, J. L. *Phys. Chem. Chem. Phys.* **2001**, *3*, 3364.
- (19) Jung, C.; Rhee, C. K. *J. Phys. Chem. B* **2005**, *109*, 8961.
- (20) Dogel, J.; Tsekov, R.; Freyland, W. *J. Chem. Phys.* **2005**, *122*.
- (21) Wu, J.-H.; Yan, J.-W.; Xie, Z.-X.; Xue, Q.-K.; Mao, B.-W. *J. Phys. Chem. B* **2004**, *108*, 2773.
- (22) Mårtensson, P.; Feenstra, R. M. *Phys. Rev. B* **1989**, *39*, 7744.
- (23) Vurgaftman, I.; Meyer, J. R.; Ram-Mohan, L. R. *J. Appl. Phys.* **2001**, *89*, 5815.
- (24) Zell, C. A.; Freyland, W. *Chem. Phys. Lett.* **2001**, *337*, 293.
- (25) Zell, C. A.; Freyland, W. *Langmuir* **2003**, *19*, 7445.